

Computational Modeling of Electro-Elasto-Capillary Phenomena in Dielectric Elastomers

Saman Seifi^a, Harold S. Park^b

^a*Department of Mechanical Engineering, Boston University, Boston, MA 02215*

^b*Department of Mechanical Engineering, Boston University, Boston, MA 02215*

Abstract

We present a new finite deformation, dynamic finite element model that incorporates surface tension to capture elastocapillary effects on the electromechanical deformation of dielectric elastomers. We demonstrate the significant effect that surface tension can have on the deformation of dielectric elastomers through three numerical examples: (1) surface tension effects on the deformation of single finite elements with homogeneous and inhomogeneous boundary conditions; (2) surface tension effects on instabilities in constrained dielectric elastomer films, and (3) surface tension effects on bursting drops in solid dielectrics. Generally, we find that surface tension creates a barrier to instability nucleation. Specifically, we find in agreement with recent experimental studies of constrained dielectric elastomer films a transition in the surface instability mechanism depending on the elastocapillary length. The present results indicate that the proposed methodology may be beneficial in studying the electromechanical deformation and instabilities for dielectric elastomers in the presence of surface tension.

Keywords: dielectric elastomer, elastocapillary

1. Introduction

Dielectric elastomers (DEs) have attracted significant attention in recent years as a soft and flexible actuation material (Carpi et al., 2010; Brochu and Pei, 2010; Biddiss and Chau, 2008). The salient characteristic of DEs is that if sandwiched between two compliant electrodes that apply voltage across its thickness, the DE can exhibit both significant thinning and in-plane expansion, where the in-plane expansion can often exceed several hundred percent (Keplinger et al., 2012). The ability to undergo such large deformations has led to DEs being studied for both actuation-based applications, including artificial muscles and flexible electronics, and also for generation-based applications and energy harvesting (Carpi et al., 2010; Brochu and Pei, 2010; Mirfakhrai et al., 2007).

Detailed studies on the mechanics of DEs began about 15 years ago with the seminal experimental work of Pelrine et al. (1998, 2000). Since then, there have been many experimental (Fox and Goulbourne, 2008; Keplinger et al., 2010; Kofod et al., 2003; Kofod and Sommer-Larsen, 2005; Pei et al., 2004; Plante and Dubowsky, 2006, 2007a,b; Schlaak et al., 2005; Wissler and Mazza, 2007; Zhang et al., 2004; Chiba et al., 2008; Wang et al., 2011, 2012b,a), theoretical (Suo et al., 2008; Suo, 2010; Goulbourne et al., 2005; Dorfmann and Ogden, 2005, 2006; McMeeking and Landis, 2005; Patrick et al., 2007; Plante and Dubowsky, 2007a,b; Wissler and Mazza, 2005), and recently a small number of computational studies (Park et al., 2012; Park and Nguyen, 2013; Park et al., 2013; Zhou et al., 2008; Zhao and Suo, 2007; Vu et al., 2007; Wissler and Mazza, 2005; Buschel et al., 2013; Khan et al., 2013; Henann et al., 2013; Li and Landis, 2012) aimed at identifying the mechanisms that have the largest impact on the nonlinear dynamical behavior and failure mechanisms of DEs. A summary of recent developments on electromechanical instabilities in DEs has been given by Zhao and Wang (2014).

URL: samansei@bu.edu (Saman Seifi), parkhs@bu.edu (Harold S. Park)

Concurrently, researchers have for many years studied the forces exerted by fluids at rest upon solids, which are known as surface tension, or elastocapillary forces. While the best-known example of surface tension is likely that of deforming liquid droplets, there has been interest in using it to deform solid structures, see the reviews of Roman and Bico (2010) and Liu and Feng (2012). Specifically, there has recently been interest in using elastocapillary forces to deform *soft* structures in controllable or unique ways, since for these systems the elastocapillary number, which is defined as $\gamma/\mu l$, where γ is the surface tension, μ is the shear modulus and l is a characteristic length, is close to unity, implying that elastocapillary effects can be substantial for these soft materials.

While elastocapillary effects have been extensively studied in soft materials, its effect on soft materials like DEs that deform when subject to an electric field, is a relatively unknown phenomenon. For example, Wang and Zhao (2013) performed interesting experiments of electrostatically deforming a constrained DE in a liquid solution, and showed that the instability mechanism of the surface could be tuned depending on the value of the surface tension. Furthermore, Pineirua et al. (2010) showed how elastocapillary origami could be developed by coupling surface tension with electric fields to deform a liquid droplet surrounded by a thin sheet of PDMS. Overall, this discussion makes clear that there may be potential in using surface tension as an additional degree of freedom to introduce new and interesting deformation mechanisms in electroactive polymers like DEs, and furthermore that the computational tools needed to investigate such phenomena are currently lacking.

Therefore, the objective of the present work is to present a finite element (FE) model for DEs accounting for the effects of surface tension, such that electro-elasto-capillary phenomena in DEs can be computationally investigated. We pay particular interest to those instances where surface tension couples to and impacts known electromechanical instabilities that dielectric elastomers are known to undergo, specifically snap-through instability (Peltine et al., 2000), surface creasing and wrinkling (Wang et al., 2011, 2012b; Wang and Zhao, 2013), and bursting drops in solid dielectrics (Wang et al., 2012a).

2. Background: Nonlinear Electromechanical Field Theory

The numerical results we present in this work are based upon a FE discretization of the electromechanical field theory proposed by Suo and co-workers (Suo et al., 2008; Suo, 2010). In this field theory at mechanical equilibrium, the nominal stress S_{iJ} satisfies the following (weak) equation:

$$\int_V S_{iJ} \frac{\partial \xi_i}{\partial X_J} dV = \int_V \left(B_i - \rho \frac{\partial^2 x_i}{\partial t^2} \right) \xi_i dV + \int_A T_i \xi_i dA, \quad (1)$$

where ξ_i is an arbitrary vector test function, B_i is the body force per unit reference volume V , ρ is the mass density of the material and T_i is the force per unit area that is applied on the surface A in the reference configuration.

For the electrostatic problem, the nominal electric displacement \tilde{D}_I satisfies the following (weak) equation:

$$- \int_V \tilde{D}_I \frac{\partial \eta}{\partial X_I} dV = \int_V q \eta dV + \int_A \omega \eta dA, \quad (2)$$

where η is an arbitrary scalar test function, q is the volumetric charge density and ω is the surface charge density, both with respect to the reference configuration. It can be seen that the strong form of the mechanical weak form in (1) is the momentum equation, while the strong form of the electrostatic weak form in (2) is Gauss's law.

As the governing field equations in (1) and (2) are decoupled, the electromechanical coupling occurs through the material laws. The hyperelastic material law we adopt here has been utilized in the literature to study the nonlinear deformations of electrostatically actuated polymers; see the works of Vu et al. (2007), and Zhao and Suo (2007). Due to the fact that the DE is a rubber-like polymer, phenomenological free energy expressions are typically used to model the deformation of the polymer chains. In the present work, we will utilize the form (Vu et al., 2007; Zhao and Suo, 2007)

$$W(\mathbf{C}, \tilde{\mathbf{E}}) = \mu W_0 - \frac{1}{2} \lambda (\ln J)^2 - 2\mu W_0 (3) \ln J - \frac{\epsilon}{2} J C_{IJ}^{-1} \tilde{E}_I \tilde{E}_J, \quad (3)$$

where W_0 is the mechanical free energy density in the absence of an electric field, ϵ is the permittivity, $J = \det(\mathbf{F})$, where \mathbf{F} is the continuum deformation gradient, C_{IJ}^{-1} are the components of the inverse of the right Cauchy-Green tensor \mathbf{C} , λ is the bulk modulus and μ is the shear modulus.

We model the mechanical behavior of the DE using the Arruda-Boyce rubber hyperelastic function (Arruda and Boyce, 1993), where the mechanical free energy W_0 in (3) is approximated by the following truncated series expansion,

$$W_0(I_1) = \frac{1}{2}(I_1 - 3) + \frac{1}{20N}(I_1^2 - 9) + \frac{11}{1050N^2}(I_1^3 - 27) + \frac{19}{7000N^3}(I_1^4 - 81) + \frac{519}{673750N^4}(I_1^5 - 243), \quad (4)$$

where N is a measure of the cross link density, I_1 is the trace of \mathbf{C} , and where the Arruda-Boyce model reduces to a Neo-Hookean model if $N \rightarrow \infty$. We note that previous experimental studies of Wissler and Mazza (2007) have validated the Arruda-Boyce model as being accurate for modeling the large deformation of DEs.

3. Finite Element Formulation

3.1. Nonlinear, Dynamic Finite Element Model

The FE model we use was previously developed by Park et al. (2012). In that work, the corresponding author and collaborators developed a nonlinear, dynamic FEM formulation of the governing nonlinear electromechanical field equations of Suo et al. (2008) that are summarized in (1) and (2). By using a standard Galerkin FE approximation to both the mechanical displacement and electric potential fields, and incorporating inertial effects in the mechanical momentum equation, an implicit, coupled, monolithic nonlinear dynamic FE formulation was obtained with the governing equations (Park et al., 2012)

$$\begin{pmatrix} \Delta \mathbf{a} \\ \Delta \Phi \end{pmatrix} = - \begin{pmatrix} \mathbf{M} + \beta \Delta t^2 \mathbf{K}^{mm} & \mathbf{K}^{me} \\ \beta \Delta t^2 \mathbf{K}^{em} & \mathbf{K}^{ee} \end{pmatrix}^{-1} \begin{pmatrix} \mathbf{R}^{mech} \\ \mathbf{R}^{elec} \end{pmatrix} \quad (5)$$

where $\Delta \mathbf{a}$ is the increment in mechanical acceleration, $\Delta \Phi$ is the increment in electrostatic potential, $\beta = 0.25$ is the standard Newmark time integrator parameter, \mathbf{R}^{mech} is the mechanical residual, \mathbf{R}^{elec} is the electrical residual, and the various stiffness matrices \mathbf{K} include the purely mechanical (\mathbf{K}^{mm}), mixed electromechanical ($\mathbf{K}^{me} = \mathbf{K}^{em}$), and purely electrostatic (\mathbf{K}^{ee}) contributions. Details regarding the residual vectors and the various mechanical, electromechanical and electrostatic stiffnesses can be found in previous work (Park et al., 2012).

In the present work, volumetric locking due to the incompressible material behavior was alleviated using the Q1P0 method of Simo et al. (1985). While viscoelastic effects have previously been accounted for within the FE model (Park and Nguyen, 2013), these effects are neglected in the present work such that the effects of surface tension on electromechanical instabilities in DEs can be investigated without other physical complications.

3.2. Surface Tension

The major computational contribution of this work is in adding surface tension effects to the FE formulation of DEs previously developed by Park et al. (2012), such that coupled electro-elasto-capillary effects can be studied. We discuss the relevant technical details in this section.

FE formulations of surface tension have been given by Saksono and Peric (2006a) and Javili and Steinmann (2010), amongst others. We note that the recently published work of Henann and Bertoldi (2014) uses the model presented by Saksono and Peric (2006a), with an incompressible hyperelastic material model for the deforming solid. In the present work, we utilize the dynamic formulation of Saksono and Peric (2006b), where the utility and importance of using inertia to capture, using FE, the electromechanical instabilities that occur in DEs was shown in the previous works of Park et al. (2012, 2013); Park and Nguyen (2013). We

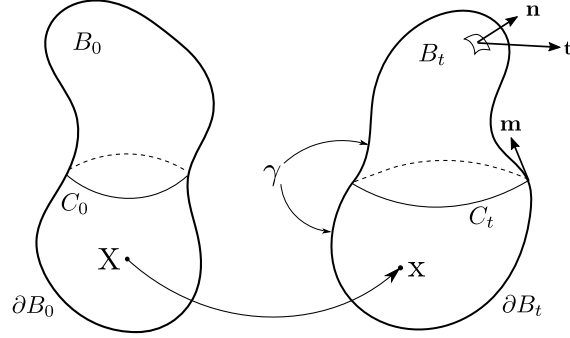


Figure 1: The reference body B_0 and the deformed body B_t at time t .

now briefly describe the formulation, and the resulting electro-elasto-capillary FE equations that we solve, while a schematic of the current and reference configurations for the large deformation kinematics is shown in Figure (1).

Using the Saksono and Peric (2006b) model, we begin with the force continuity at the solid-liquid interface,

$$\sigma \mathbf{n} = -p_{ext} \mathbf{n} + 2H\gamma \mathbf{n} \quad (6)$$

where \mathbf{n} is the unit normal, σ is the Cauchy stress, H is the mean curvature, and p_{ext} is an external pressure. The spatial (updated Lagrangian) form of the weak form of the momentum equation can then be written as

$$\begin{aligned} \int (\sigma : \nabla \mathbf{w} - \rho(\mathbf{b} - \mathbf{a}) \cdot \mathbf{w}) dv - \int \mathbf{t} \cdot \mathbf{w} da - \int (-p_{ext} \mathbf{n} \cdot \mathbf{w}) da \\ + \int (\gamma \nabla_s \cdot \mathbf{w}) da - \int (\gamma \mathbf{w} \cdot \mathbf{m}) ds = 0 \end{aligned} \quad (7)$$

where \mathbf{w} is the virtual displacement, \mathbf{t} is the traction, \mathbf{b} is the body force, $\nabla_s = (\mathbf{I} - \mathbf{n} \otimes \mathbf{n}) \nabla$ is the surface gradient operator, ρ is the density and \mathbf{a} is the acceleration. In the present work, we neglect the three-phase contact line, i.e. the integral in (7) over the line ds , for simplicity.

The FE form of (7) can be obtained by making the usual Galerkin approximation of both the displacements and virtual displacements with the same shape functions, resulting in the (mechanical) residual $\mathbf{R}^{mech}(\mathbf{X})$

$$\mathbf{R}^{mech}(\mathbf{X}) = \mathbf{M}\ddot{\mathbf{X}} + \mathbf{F}^{int} - \mathbf{F}^{ext} + \mathbf{F}^{surf} = 0 \quad (8)$$

where the various terms in (8) take the following form for each element e

$$\begin{aligned} \mathbf{M}_e &= \int \rho \mathbf{N}^T \mathbf{N} dv \\ \mathbf{F}_e^{int} &= \int \mathbf{B}^T \sigma dv \\ \mathbf{F}_e^{ext} &= \int \mathbf{N}^T \mathbf{b} dv + \int \mathbf{N}^T \mathbf{t} da \\ \mathbf{F}_e^{surf} &= \int \gamma \nabla_s \mathbf{N} da \end{aligned} \quad (9)$$

where \mathbf{N} and \mathbf{B} are the standard FE shape function and gradient, respectively. As can be seen in (8), the only non-standard term compared to the standard discretization of the momentum equation arises in the surface force \mathbf{F}^{surf} , and the corresponding surface stiffness \mathbf{K}^{surf} .

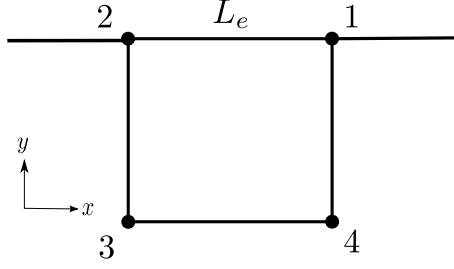


Figure 2: Schematic of finite element nodal numbering consistent with surface tension formulation given in Eqs. (10) and (11). Nodes 1 and 2 are surface nodes.

Henann and Bertoldi (2014) analytically derived the surface force \mathbf{F}^{surf} for a two-dimensional, 4-node bilinear quadrilateral element as

$$\mathbf{F}^{surf} = -\frac{h\gamma}{L_e} \begin{pmatrix} x_1 - x_2 \\ y_1 - y_2 \\ x_2 - x_1 \\ y_2 - y_1 \end{pmatrix} \quad (10)$$

The surface stiffness \mathbf{K}^{surf} can be obtained through linearization of the surface force \mathbf{F}^{surf} in (8). This value for a 4-node bilinear quadrilateral element in two-dimensions was also given analytically by Henann and Bertoldi (2014) as

$$\mathbf{K}^{surf} = \frac{h\gamma}{L_e} \begin{pmatrix} 1 & 0 & -1 & 0 \\ 0 & 1 & 0 & -1 \\ -1 & 0 & 1 & 0 \\ 0 & -1 & 0 & 1 \end{pmatrix} - \frac{h\gamma}{L_e^3} \begin{pmatrix} x_1 - x_2 \\ y_1 - y_2 \\ x_2 - x_1 \\ y_2 - y_1 \end{pmatrix} \begin{pmatrix} x_1 - x_2 \\ y_1 - y_2 \\ x_2 - x_1 \\ y_2 - y_1 \end{pmatrix}^T \quad (11)$$

where $L_e = \sqrt{(x_2 - x_1)^2 + (y_2 - y_1)^2}$ is the length of the FE face containing nodes 1 and 2. The ordering of the FE nodes corresponding to Eqs. (10) and (11) is shown in Figure (2).

The final coupled electromechanical FE equations we solve, which include the surface tension terms, can be written as

$$\begin{pmatrix} \Delta \mathbf{a} \\ \Delta \Phi \end{pmatrix} = - \begin{pmatrix} \mathbf{M} + \beta \Delta t^2 (\mathbf{K}^{mm} + \mathbf{K}^{surf}) & \mathbf{K}^{me} \\ \beta \Delta t^2 \mathbf{K}^{em} & \mathbf{K}^{ee} \end{pmatrix}^{-1} \begin{pmatrix} \mathbf{R}^{mech} \\ \mathbf{R}^{elec} \end{pmatrix} \quad (12)$$

In comparing the new FE formulation including surface tension in (12) to the previous FE equations of Park et al. (2012) in (5), the only changes are the addition of the surface stiffness \mathbf{K}^{surf} to the standard mechanical stiffness matrix \mathbf{K}^{mm} , as well as the surface contribution \mathbf{F}^{surf} to the mechanical residual \mathbf{R}^{mech} , as shown previously in (8) and (9).

4. Numerical Results

All numerical simulations were performed using the open source simulation code Tahoe (2015) using standard 4-node, bilinear quadrilateral finite elements within a two-dimensional, plane strain approximation. Before any application of electrostatic loading via applied voltages, the surface tension is first applied incrementally until the desired value is reached. This incremental approach is necessary to avoid computational instabilities, as previously discussed by Javili and Steinmann (2010). The surface tension is applied incrementally by first defining a target value of surface tension γ , after which we define the following function for the current value of surface tension γ_0 :

$$\gamma_0 = \min \left(\gamma, \frac{\gamma t}{t_0} \right) \quad (13)$$

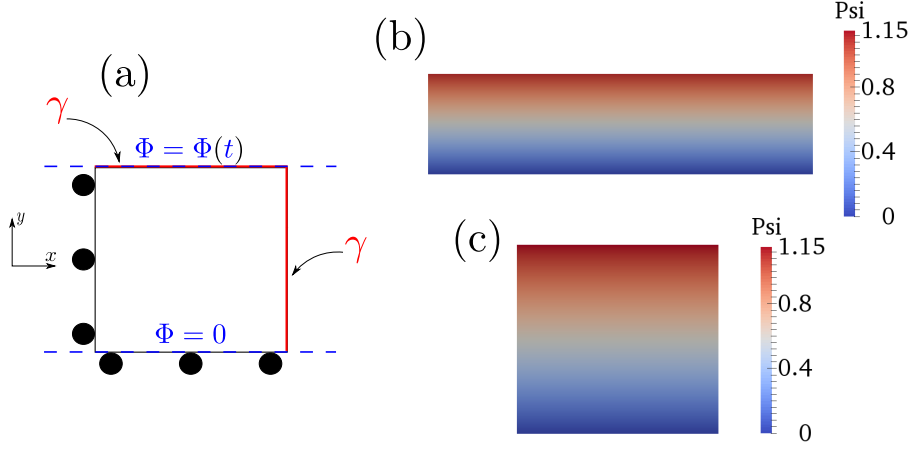


Figure 3: (a) Schematic of a single finite element with homogeneous boundary conditions; (b) Deformed configuration with $\gamma/\mu l = 0$; (c) Deformed configuration with $\gamma/\mu l = 10$. Note that Psi in (b) and (c) refers to voltage.

where t is the current time and t_0 is the total time allotted to reach the prescribed value for surface tension γ . Once the system is in equilibrium with the surface tension, voltage is applied in a monotonically increasing fashion.

4.1. Single Element Tests

We first perform a suite of parametric benchmark studies to gain a qualitative understanding of how surface tension impacts the electromechanical behavior of DEs undergoing homogeneous and inhomogeneous deformation. A single 4-node bilinear quadrilateral element of unit length and height is used for these simulations. For all numerical simulations, we chose the following constitutive parameters for the Arruda-Boyce model in Eq. (4): $\mu = \epsilon = 1$, $\lambda = 1000$ and $N = 5.0$, while different values of the surface tension γ are chosen.

4.1.1. Homogeneous Deformation

The first set of boundary conditions are to allow homogeneous deformation of the DE. The electromechanical boundary conditions are as shown in Fig. (3)(a), with rollers on the -x and -y surfaces, and voltage applied at the top surface of the single square element. Surface tension is present on the free surfaces. The resulting configurations for elastocapillary number values of $\gamma/\mu l = 0$ and $\gamma/\mu l = 10$ are shown in Figures (3)(b) and (c). As can be seen, Figure (3)(b) shows the well-known deformed configuration where the DE contracts along the thickness direction while simultaneously elongating in response to the applied voltage, thus exhibiting the well-known electromechanical snap through instability (Park et al., 2012). However, the configuration in Figure (3)(c) is quite different when $\gamma/\mu l = 10$. Instead of resulting in a rectangular deformed configuration, the single element takes a deformed configuration that is not much changed from the initial, square configuration, which shows that the impact of surface tension is to resist the deformation that would otherwise occur due to the applied voltage.

We plot the resulting normalized voltage-charge curves in Figure (4) for various values of $\gamma/\mu l$. We can see that the effect of increasing surface tension is to significantly increase the voltage that is required to induce the electromechanical instability. These results are quantitatively in agreement with previous experimental and theoretical studies on soft materials which found that the effect of surface tension is to create a barrier to instability nucleation (Chen et al., 2012; Mora et al., 2011). We also note that a softening response is not observed in the voltage-charge plot due the fact that a plane strain, and not plane stress (Zhou et al., 2008) approximation in two dimensions is utilized.

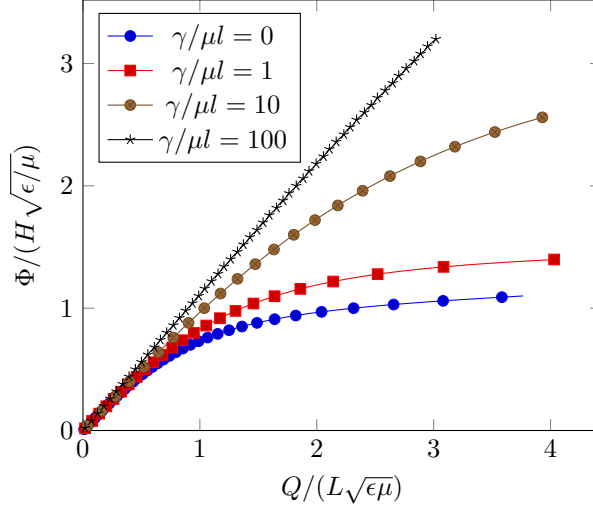


Figure 4: Deformation of a single, homogeneously deforming finite element subject to voltage loading.

4.1.2. Inhomogeneous Deformation

Before studying surface tension effects on inhomogeneously deforming DEs, as will be done in subsequent computational examples, we first study a single FE that is fully constrained mechanically along its bottom surface, as illustrated in Figure (5)(a), where surface tension is present on the free surfaces. If no surface tension is present, i.e. $\gamma/\mu l = 0$, the top surface of the element bows outward in response to the applied voltage as seen in Figure (5)(b). However, for non-zero surface tension $\gamma/\mu l = 10$, the large outward bowing of the top surface that was observed for $\gamma/\mu l = 0$ in Figure (5)(b) is reduced drastically, as shown in Figure (5)(c). The effect of the surface tension opposing the deformation that is induced by the voltage is similar to that previously observed for the homogeneous boundary conditions.

We also analyze the voltage-charge curve for different values of $\gamma/\mu l$ in Figure (6). As can be seen, the major effect of surface tension is again to significantly increase the value of voltage Φ that is required in order to induce the voltage-induced electromechanical snap-through instability.

4.2. Surface Creasing in Constrained 2D Strip

Our next example is based on recent experiments by Wang and Zhao (2013), who studied the surface instability mechanisms in constrained DE films in which the top surface is immersed in a fluid. The fluid was varied such that the top surface of the DE film was subject to different values of surface tension. Interestingly, upon application of a critical voltage, a transition in the surface instability mechanism from creasing to wrinkling was observed, which was found to be dependent on elastocapillary length $\gamma/(\mu H)$, where H is the film thickness. Along with the transition in surface instability mechanism, the wavelength of the instability was also found to change, from about $\lambda = 1.5H$ for the creasing instability to longer wavelengths, $\lambda = 5 - 12H$ when the elastocapillary length $\gamma/(\mu H) > 1$.

We performed FE simulations of the experiments of Wang and Zhao (2013), where the schematic of the problem geometry and the relevant electro-elasto-capillary boundary conditions is shown in Figure (7), i.e. the bottom surface of the film is fixed, the left and right sides are on rollers while a voltage is applied to the top surface, where the surface tension is also present. Most results shown are for a DE film of dimensions 160×4 , which was discretized with square 4-node bilinear quadrilateral finite elements having an edge length of unity.

We show in Figure (8)(a) the difference in surface instability mechanism depending on the elastocapillary length. As can be seen, when the elastocapillary length is small (i.e. $\gamma/\mu H = 0.5$), the surface instability mechanism is that of creasing, or localized folds, as previously observed both experimentally (Wang et al.,

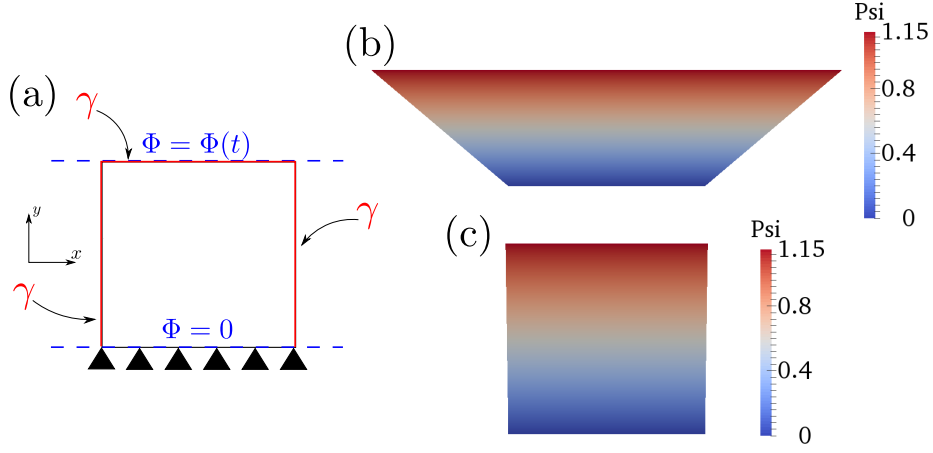


Figure 5: (a) Schematic of single finite element with inhomogeneous boundary conditions; (b) Deformed configuration with $\gamma/\mu l = 0$; (c) Deformed configuration with $\gamma/\mu l = 10$. Note that Psi in (b) and (c) refers to voltage.

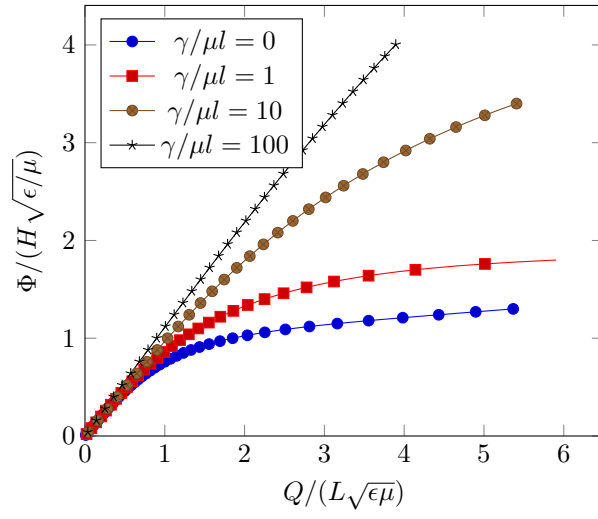


Figure 6: Deformation of a single, inhomogeneously deforming finite element subject to voltage loading.

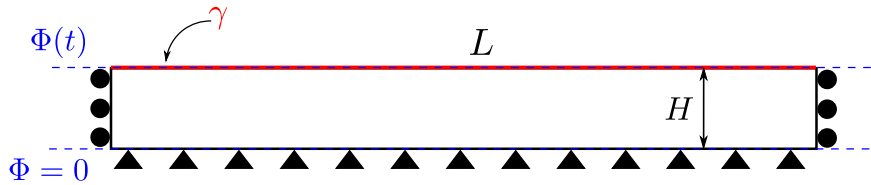


Figure 7: Schematic of the DE film with electro-elasto-capillary boundary conditions.

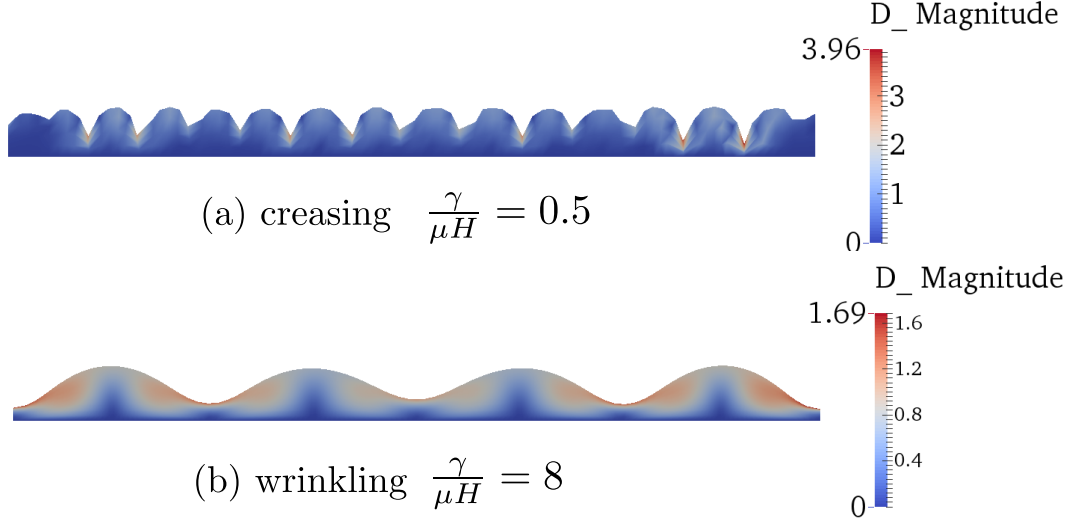


Figure 8: Computationally observed transition in the surface instability mechanism in DEs as a function of the elastocapillary length $\gamma/(\mu H)$, for a DE film of dimensions 80×4 . The variable $D_Magnitude$ refers to the magnitude of the displacement field.

2011), and computationally (Park et al., 2013). As the elastocapillary length increases to become similar to the film height, the surface instability mechanism changes to wrinkling, as shown in Figure (8)(b). The change in instability mechanism is characterized by a significantly larger instability wavelength as compared to the creasing instability in Figure (8)(a). Furthermore, rather than abrupt, localized folds as in the creasing instability in Figure (8)(a), the surface exhibits a more gradual and undulating pattern as seen in Figure (8)(b).

This instability transition was also characterized experimentally by plotting the normalized electric field $E_c/\sqrt{\mu/\epsilon}$ as a function of the elastocapillary length, as shown in Figure (9), where E_c is the value of the electric field when the instability nucleates. The analytic solutions for the critical electric fields to nucleate wrinkles and creases were developed by Wang and Zhao (2013), and are written as:

$$E_{crease}^c \approx 1.03 \sqrt{\frac{\mu}{\epsilon}} + 1.88 \sqrt{\frac{\gamma}{H\epsilon}} \quad (14)$$

$$E_{wrinkle}^c \approx 2.49 \sqrt{\frac{\mu}{\epsilon}} + 0.46 \sqrt{\frac{\gamma}{H\epsilon}} \quad (15)$$

As seen in Figure (9), the FE model is able to capture the general trends, including the transition in the value of the critical electric field E_c predicted theoretically. The FE prediction for the critical electric field is generally larger than the analytic theory, which is expected given that while a locking-resistant Q1P0 formulation was used Simo et al. (1985), the FE-discretized structure is still stiffer than the continuum.

We also calculated the normalized instability wavelength λ/H as a function of the elastocapillary length as shown in Figure (10). In that figure, the wrinkling wavelength as a function of elastocapillary number is given by

$$\frac{\epsilon E^2}{\mu} = 2Hk \frac{1 + 2e^{2Hk} + e^{4Hk} + 4e^{2Hk}H^2k^2}{-1 + e^{4Hk} - 4e^{2Hk}Hk} + (Hk)^2 \frac{\gamma}{\mu H} \quad (16)$$

The creasing wavelength is fixed as $\lambda_{crease} = 1.5H$, which was previously obtained by Wang and Zhao (2013).

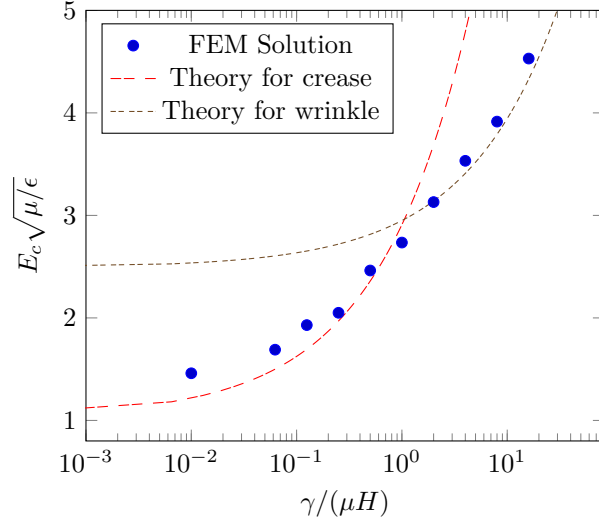


Figure 9: Normalized critical electrical field as a function of elastocapillary length for a 160x4 DE film.

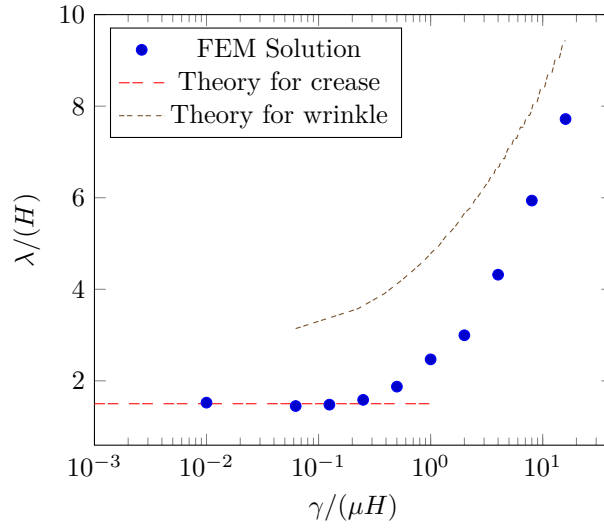


Figure 10: Normalized instability wavelength as a function of elastocapillary length for a 160x4 DE film.

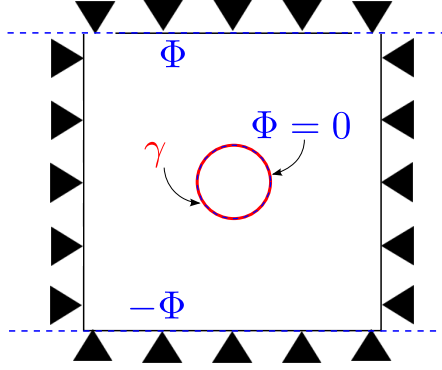


Figure 11: Computational model for bursting drop in dielectric elastomer.

For elastocapillary numbers $\gamma/(\mu H) < 1$, we find the normalized wavelength λ/H to be close to the value of 1.5 predicted theoretically Wang and Zhao (2013). For larger elastocapillary numbers, i.e. $\gamma/(\mu H) > 1$, where wrinkling is observed, a dramatic increase in normalized instability wavelength λ/H is observed. While our FE simulations capture the instability wavelength transition, the predicted wavelength after the transition to wrinkling occurs is smaller than the analytic theory.

This discrepancy was also observed in the experimental studies of Wang and Zhao (2013). In that work, like the current FE models, the critical electric fields for creasing and wrinkling as in Figure (9) were in better agreement with the analytic theory than the instability wavelength. Specifically, the experiments also found a smaller instability wavelength in the transition region from creasing to wrinkling than the analytic solution. The FE predictions do fall within the bounds observed experimentally by Wang and Zhao (2013), though at the lower end of the observed wavelengths. This is likely due to differences in how the instability wavelength was calculated in our plane strain 2D FE simulations as compared to the 3D experimental studies. In particular, there is larger spatial variation in the wavelengths observed in the 3D experimental structure, whereas the 2D plane strain approximation results in a constant instability wavelength through the thickness of the film, and so we expect and find that the FE predictions fall towards the lower end of the experimental values.

4.3. Bursting drop in a solid dielectric

Our final numerical example is a computational study of the experiments of Wang et al. (2012a). The experimental configuration is shown in Figure (11). The problem is one of a dielectric film with a small hole containing a conductive liquid, for example NaCl solution. All edges of the film are constrained mechanically, and a voltage differential Φ is applied across the film. The novel experimental finding was the first observation of instabilities of drops in solids, in which the drop in the center of the film begins to elongate in a crack-like fashion towards the boundaries at which the voltage is applied. While viscoelastic effects on the bursting drop instability were previously studied by Park and Nguyen (2013), what has not been investigated, either experimentally or theoretically, is the effect of changing the conductive fluid within the hole. We account for the effect of different conductive fluids by changing the surface tension around the hole perimeter, as shown schematically in Figure (11).

The 2D plane strain model in Figure (11) had dimensions of 20 by 20, with the radius of the hole being 2. The geometry was discretized using 4-node bilinear quadrilateral finite elements with a mesh spacing of 0.25, for a total number of 6271 elements and 6456 nodes.

The electromechanical instability is shown in Figure (12). There, it is seen that as the applied voltage increases, the circular drop begins to change shape, and then as shown in Figures (12)(b)-(d), begins to elongate in the direction of the applied voltage, where the elongation resembles crack-like propagation.

We quantify the effects of surface tension on the nature of the bursting drop. We show in Figure (13) three snapshots, overlaid on top of each other, of the bursting drop geometry taken at the same time for

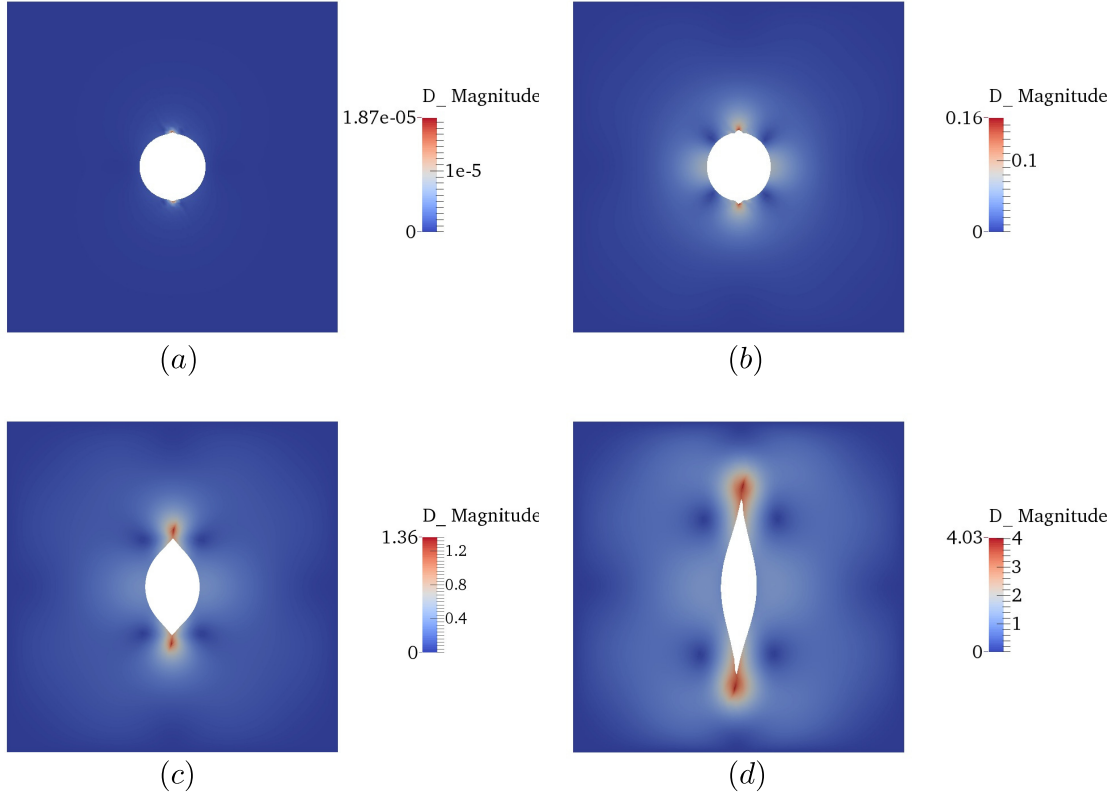


Figure 12: Representative snapshots of [\[hsp: bursting drop evolution\]](#) in constrained DE film.

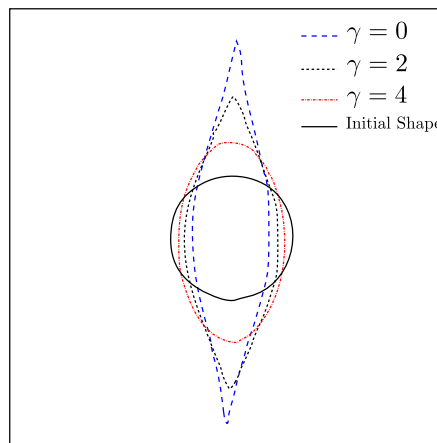


Figure 13: Snapshot of bursting drop geometry taken at same time for different values of surface tension γ .

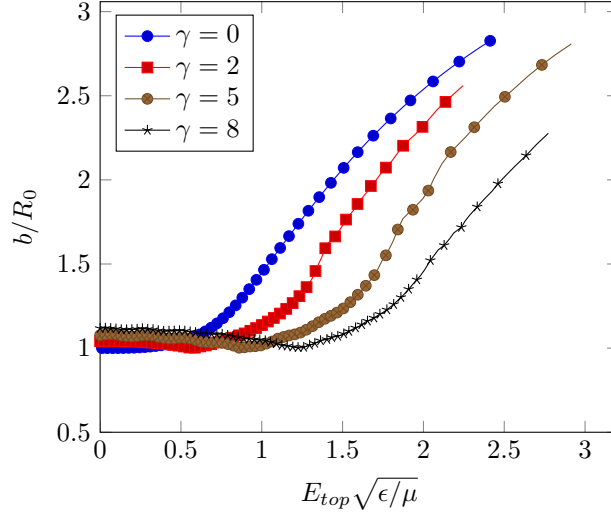


Figure 14: Position of bursting drop tip as a function of applied electric field E_{top} , where R_0 is the initial radius of the drop, and b is the long axis of the bursting drop.

different values of surface tension γ . As can be seen, the drop has elongated the most for the case without surface tension, i.e. $\gamma = 0$ as compared to its initial, circular shape. As the surface tension increases, the bursting drop elongation becomes progressively more delayed, which again shows that surface tension acts as a barrier to instability nucleation in electroactive polymers. *[hsp: We also note that the slightly asymmetric direction of bursting drop elongation is due to the fact that bursting drop follows the contours of the FE mesh, which is slightly asymmetric with respect to the hole.]*

[hsp: It is also of interest to quantify the position of the bursting drop tip as a function of applied electric field, which is shown in Figure (14). As can be seen, the nucleation for larger values of surface tension is delayed, and thus occurs at larger values of applied electric field E_{top} . Once the nucleation occurs, and the bursting drop begins to elongate towards the applied electric field, it appears as though the surface tension does not have a significant impact on the elongation rate of the bursting drop tip, which is in contrast to the effect that viscoelasticity was previously observed to have (Park and Nguyen, 2013). This is likely because viscoelasticity impacts the stiffness of the entire DE geometry, whereas the surface tension creates a nucleation barrier only at the bursting drop tip.]

5. Conclusions

We have presented a new dynamic, finite deformation finite element model of dielectric elastomers that incorporates surface tension to capture elastocapillary effects on the electromechanical deformation. The simulations demonstrate that increasing surface tension, or equivalently the elastocapillary number, results in an increase in the critical voltage or electric field needed to nucleate an electromechanical instability in the dielectric elastomer. We also demonstrated a transition in surface instability mechanism from creasing to wrinkling in constrained dielectric elastomer films by increasing the elastocapillary number. The present results indicate that the proposed methodology may be beneficial in studying the electromechanical deformation and instabilities for dielectric elastomers in the presence of surface tension.

6. Acknowledgements

HSP and SS acknowledge funding from the ARO, grant W911NF-14-1-0022.

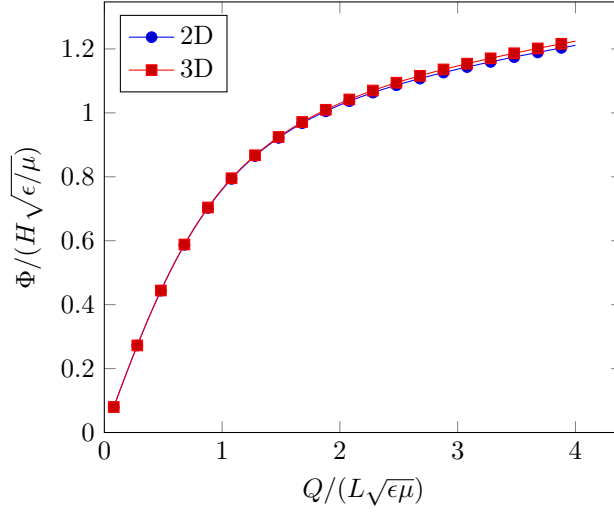


Figure 15: Comparison of 2D and constrained 3D results for inhomogeneous deformation of a single finite element.

7. Appendix

We show here verification of the 2D Q1P0 formulation in alleviating volumetric locking. To do so, we compare it to results obtained using a single 8-node hexahedral element with the previously published Q1P0 formulation of Park et al. (2013). The 2D results were obtained using the 2D version of the Q1P0 formulation of Simo et al. (1985); the boundary conditions on the single 4-node quadrilateral 2D finite element were the same as those previously seen in Figure (5)(a). For the 3D element, in addition to having its bottom surface completely constrained, all z -displacements were set to zero to mimic a 2D plane strain problem.

The results are shown in Figure (15). As can be seen, the 2D and constrained 3D formulations give quite similar results, validating the present 2D formulation.

References

- Arruda, E.M., Boyce, M.C., 1993. A three-dimensional constitutive model for the large stretch behavior of rubber elastic materials. *Journal of the Mechanics and Physics of Solids* 41, 389–412.
- Biddiss, E., Chau, T., 2008. Dielectric elastomers as actuators for upper limb prosthetics: challenges and opportunities. *Medical Engineering and Physics* 30, 403–418.
- Brochu, P., Pei, Q., 2010. Advances in dielectric elastomers for actuators and artificial muscles. *Macromolecular Rapid Communications* 31, 10–36.
- Buschel, A., Klinkel, S., Wagner, W., 2013. Dielectric elastomers - numerical modeling of nonlinear visco-electroelasticity. *International Journal for Numerical Methods in Engineering* 93, 834–856.
- Carpi, F., Bauer, S., Rossi, D.D., 2010. Stretching dielectric elastomer performance. *Science* 330, 1759–1761.
- Chen, D., Cai, S., Suo, Z., Hayward, R.C., 2012. Surface energy as a barrier to creasing of elastomer films: an elastic analogy to classical nucleation. *Physical Review Letters* 109, 038001.
- Chiba, S., Waki, M., Kornbluh, R., Pelrine, R., 2008. Innovative power generators for energy harvesting using electroactive polymer artificial muscles. *Proceedings of the SPIE* 6927, 692715.
- Dorfmann, A., Ogden, R.W., 2005. Nonlinear electroelasticity. *Acta Mechanica* 82, 99–127.
- Dorfmann, A., Ogden, R.W., 2006. Nonlinear electroelastic deformations. *Journal of Elasticity* 174, 167–183.
- Fox, J.W., Goulbourne, N.C., 2008. On the dynamic electromechanical loading of dielectric elastomer membranes. *Journal of the Mechanics and Physics of Solids* 56, 2669–2686.
- Goulbourne, N.C., Mockensturm, E.M., Frecker, M.I., 2005. A nonlinear model for dielectric elastomer membranes. *Journal of Applied Mechanics* 72, 899–906.
- Henann, D.L., Bertoldi, K., 2014. Modeling of elasto-capillary phenomena. *Soft Matter* 10, 709–717.
- Henann, D.L., Chester, S.A., Bertoldi, K., 2013. Modeling of dielectric elastomers: design of actuators and energy harvesting devices. *Journal of the Mechanics and Physics of Solids* 61, 2047–2066.
- Javili, A., Steinmann, P., 2010. A finite element framework for continua with boundary energies. part II: the three-dimensional case. *Computer Methods in Applied Mechanics and Engineering* 199, 755–765.

- Keplinger, C., Kaltenbrunner, M., Arnold, N., Bauer, S., 2010. Röntgen's electrode-free elastomer actuators without electromechanical pull-in instability. *Proceedings of the National Academy of Science* 107, 4505–4510.
- Keplinger, C., Li, T., Baumgartner, R., Suo, Z., Bauer, S., 2012. Harnessing snap-through instability in soft dielectrics to achieve giant voltage-triggered deformation. *Soft Matter* 8, 285–288.
- Khan, K.A., Wafai, H., Sayed, T.E., 2013. A variational constitutive framework for the nonlinear viscoelastic response of a dielectric elastomer. *Computational Mechanics* 52, 345–360.
- Kofod, G., Sommer-Larsen, P., 2005. Silicone dielectric elastomer actuators: finite-elasticity model of actuation. *Sensors and Actuators A* 122, 273–283.
- Kofod, G., Sommer-Larsen, P., Kornbluh, R., Pelrine, R., 2003. Actuation response of polyacrylate dielectric elastomers. *Journal of Intelligent Material Systems and Structures* 14, 787–793.
- Li, W., Landis, C.M., 2012. Deformation and instabilities in dielectric elastomer composites. *Smart Materials and Structures* 21, 094006.
- Liu, J.L., Feng, X.Q., 2012. On elastocapillarity: a review. *Acta Mechanica Sinica* 28, 928–940.
- McMeeking, R.M., Landis, C.M., 2005. Electrostatic forces and stored energy for deformable dielectric materials. *Journal of Applied Mechanics* 72, 581–590.
- Mirfakhrai, T., Madden, J.D.W., Baughman, R.H., 2007. Polymer artificial muscles. *Materials Today* 10, 30–38.
- Mora, S., Abkarian, M., Tabuteau, H., Pomeau, Y., 2011. Surface instability of soft solids under strain. *Soft Matter* 7, 10612–10619.
- Park, H.S., Nguyen, T.D., 2013. Viscoelastic effects on electromechanical instabilities in dielectric elastomers. *Soft Matter* 9, 1031–1042.
- Park, H.S., Suo, Z., Zhou, J., Klein, P.A., 2012. A dynamic finite element method for inhomogeneous deformation and electromechanical instability of dielectric elastomer transducers. *International Journal of Solids and Structures* 49, 2187–2194.
- Park, H.S., Wang, Q., Zhao, X., Klein, P.A., 2013. Electromechanical instability on dielectric polymer surface: modeling and experiment. *Computer Methods in Applied Mechanics and Engineering* 260, 40–49.
- Patrick, L., Gabor, K., Silvain, M., 2007. Characterization of dielectric elastomer actuators based on a hyperelastic film model. *Sensors and Actuators A* 135, 748–757.
- Pei, Q., Pelrine, R., Rosenthal, M., Stanford, S., Prahlad, H., Kornbluh, R., 2004. Recent progress on electroelastomer artificial muscles and their application for biomimetic robots. *Proceedings of the SPIE* 5385, 41–50.
- Pelrine, R., Kornbluh, R., Pei, Q., Joseph, J., 2000. High-speed electrically actuated elastomers with strain greater than 100%. *Science* 287, 836–839.
- Pelrine, R.E., Kornbluh, R.D., Joseph, J.P., 1998. Electrostriction of polymer dielectrics with compliant electrodes as a means of actuation. *Sensors and Actuators A* 64, 77–85.
- Pineirua, M., Bico, J., Roman, B., 2010. Capillary origami controlled by an electric field. *Soft Matter* 6, 4491–4496.
- Plante, J.S., Dubowsky, S., 2006. Large-scale failure modes of dielectric elastomer actuators. *International Journal of Solids and Structures* 43, 7727–7751.
- Plante, J.S., Dubowsky, S., 2007a. On the performance mechanisms of dielectric elastomer actuators. *Sensors and Actuators A* 137, 96–109.
- Plante, J.S., Dubowsky, S., 2007b. On the properties of dielectric elastomer actuators and their design implications. *Smart Materials and Structures* 16, S227–S236.
- Roman, B., Bico, J., 2010. Elasto-capillarity: deforming an elastic structure with a liquid droplet. *Journal of Physics: Condensed Matter* 22, 493101.
- Saksono, P.H., Peric, D., 2006a. On finite element modelling of surface tension. variational formulation and applications - part I: quasistatic problems. *Computational Mechanics* 38, 265–281.
- Saksono, P.H., Peric, D., 2006b. On finite element modelling of surface tension. variational formulation and applications - part II: dynamic problems. *Computational Mechanics* 38, 251–263.
- Schlaak, H.F., Jungmann, M., Matysek, M., Lotz, P., 2005. Novel multilayer electrostatic solid-state actuators with elastic dielectric. *Proceedings of the SPIE* 5759, 121–133.
- Simo, J.C., Taylor, R.L., Pister, K.S., 1985. Variational and projection methods for the volume constraint in finite deformation elasto-plasticity. *Computer Methods in Applied Mechanics and Engineering* 51, 177–208.
- Suo, Z., 2010. Theory of dielectric elastomers. *Acta Mechanica Solida Sinica* 23, 549–578.
- Suo, Z., Zhao, X., Greene, W.H., 2008. A nonlinear field theory of deformable dielectrics. *Journal of the Mechanics and Physics of Solids* 56, 467–486.
- Tahoe, 2015. <http://sourceforge.net/projects/tahoe/>.
- Vu, D.K., Steinmann, P., Possart, G., 2007. Numerical modelling of non-linear electroelasticity. *International Journal for Numerical Methods in Engineering* 70, 685–704.
- Wang, Q., Suo, Z., Zhao, X., 2012a. Bursting drops in solid dielectrics caused by high voltages. *Nature Communications* 3, 1157.
- Wang, Q., Tahir, M., Zang, J., Zhao, X., 2012b. Dynamic electrostatic lithography: multiscale on-demand patterning on large-area substrates. *Advanced Materials* 24, 1947–1951.
- Wang, Q., Zhang, L., Zhao, X., 2011. Creasing to cratering instability in polymers under ultrahigh electric fields. *Physical Review Letters* 106, 118301.
- Wang, Q., Zhao, X., 2013. Creasing-wrinkling transition in elastomer films under electric fields. *Physical Review E* 88, 042403.
- Wissler, M., Mazza, E., 2005. Modeling and simulation of dielectric elastomer actuators. *Smart Materials and Structures* 14, 1396–1402.

- Wissler, M., Mazza, E., 2007. Mechanical behavior of an acrylic elastomer used in dielectric elastomer actuators. *Sensors and Actuators A* 134, 494–504.
- Zhang, X.Q., Wissler, M., Jaehne, B., Broennimann, R., Kovacs, G., 2004. Effects of crosslinking, prestrain and dielectric filler on the electromechanical response of a new silicone and comparison with acrylic elastomer. *Proceedings of the SPIE* 5385, 78–86.
- Zhao, X., Suo, Z., 2007. Method to analyze electromechanical instability of dielectric elastomers. *Applied Physics Letters* 91, 061921.
- Zhao, X., Wang, Q., 2014. Harnessing large deformation and instabilities of soft dielectrics: theory, experiment, and application. *Applied Physics Reviews* 1, 021304.
- Zhou, J., Hong, W., Zhao, X., Zhang, Z., Suo, Z., 2008. Propagation of instability in dielectric elastomers. *International Journal of Solids and Structures* 45, 3739–3750.